One-dimensional electric field structure of an outer gap accelerator – II. γ-ray production resulting from inverse Compton scattering

K. Hirotani[1]★ and S. Shibata[2]

[1]*National Astronomical Observatory, Osawa, Mitaka, Tokyo 181-8588, Japan*
[2]*Department of Physics, Yamagata University, Yamagata 990-8560, Japan*

ABSTRACT

We study the structure of a stationary and axisymmetric charge-deficient region (or a potential gap) in the outer magnetosphere of a spinning neutron star. A large electric field along the magnetic field lines is created in this potential gap and accelerates migratory electrons (e^-) and/or positrons (e^+) to ultrarelativistic energies. Assuming that the gap is immersed in a dense soft photon field, these relativistic $e^\pm$ radiate γ-ray photons via inverse Compton (IC) scattering. These γ-rays, in turn, produce yet more radiating particles by colliding with ambient soft photons, leading to a pair-production cascade in the gap. The replenished charges partially screen the longitudinal electric field, which is self-consistently solved together with the distribution of $e^\pm$ and γ-ray photons. It is demonstrated that the voltage drop in the gap is not more than 10^{10} V when the background X-ray radiation is as luminous as $10^{37}\,\mathrm{erg\,s^{-1}}$. However, this value increases with decreasing X-ray luminosity and attains 10^{12} V when the X-ray radiation is $10^{36}\,\mathrm{erg\,s^{-1}}$. In addition, we find useful expressions of the spatial distribution of the particle fluxes and longitudinal electric field, together with the relationship between the voltage drop and the current density. Amazingly, these expressions are valid not only when IC scattering dominates but also when curvature radiation dominates.

Key words: magnetic fields – pulsars: general – gamma-rays: theory.

1 INTRODUCTION

The study of pair plasma production in a pulsar outer magnetosphere is astrophysically interesting in the context of high-energy emission from isolated spin-powered pulsars. If the magnetosphere is filled with a plasma so that the space charge density ρ_e is equal to the Goldreich–Julian charge density [$\rho_{GJ} \equiv \Omega B_z/(2\pi c)$ in the non-relativistic limit, Goldreich & Julian 1969], then the field-aligned electric field vanishes by definition, where B_z is the component of the magnetic field along the rotational axis. However, the depletion of charge in the Goldreich & Julian model in a region where it cannot be resupplied may cause a vacuum region to develop. Holloway (1973) pointed out the possibility that a region that lacks plasma is formed around the surface on which the Goldreich–Julian density ρ_{GJ} changes its sign.

Chen, Ho & Ruderman (1986a,b hereafter CHR) developed a version of the outer magnetospheric γ-ray emission zone in which acceleration in the Holloway gaps brings the particles to large Lorentz factors ($\sim 10^{7.5}$). These primary particles produce high-energy γ-ray photons, some (or most) of which collide with soft photons to materialize as secondary pairs. The resulting secondary

charges suffer strong synchrotron losses to emit secondary radiation. The secondary photons, in turn, materialize as low-energy tertiary pairs, which were argued to produce the soft tertiary photon bath needed for the original gap closure.

However, few attempts have so far been made at the construction of self-consistent electrodynamic structure for outer gap models. For example, CHR assumed a uniform potential drop so that the acceleration field was $\sim V_{gap}/r_{LC}$, where V_{gap} is the voltage drop in the gap and r_{LC} is the light cylinder radius. For a spinning neutron star with angular frequency Ω (rad s^{-1}), r_{LC} is given by

$$r_{LC} = \frac{c}{\Omega} = 10^{8.5}\Omega_2^{-1}\,\mathrm{cm}, \tag{1}$$

where $\Omega_2 \equiv \Omega/10^2\,\mathrm{rad\,s^{-1}}$, and c is the speed of light. Subsequently, Romani (1996) assumed its functional form as $\sim r^{-1}$ and computed γ-ray pulse profiles, spectra, and so on. It was Hirotani & Shibata (1998, hereafter Paper I) who first solved the spatial distribution of $E_\parallel$ explicitly together with those of particles ($e^\pm$) and γ-ray distribution functions, by solving the Poisson equation and the Boltzmann equations of $e^\pm$s and γ-ray photons self-consistently (see also Beskin, Istomin & Par'ev 1992; Hirotani

★ E-mail: hirotani@hotaka.mtk.nao.ac.jp

& Okamoto 1998 for the same method applied for a black hole magnetosphere). They considered an outer gap immersed in a relatively low-luminosity background radiation field, in which curvature radiation contributes to γ-ray production.

In this paper, we extend the method proposed in Paper I to a magnetosphere that is immersed in a luminous photon field in which inverse Compton (IC) scatterings are the dominant process for γ-ray production (Fig. 1). In the next section, we present basic equations describing the system. We then solve these equations in Section 3 and reveal quantitative characteristics of the pair-production cascade. In this paper, we assume an aligned rotator for simplicity. Some authors, however, think that aligned rotators are inactive with static electrosphere (Michel 1998), and this issue is controversial. Nevertheless, the present model is generic in the sense that what we consider is the dynamics around the null surface when the current pierces through it; therefore, the result is applicable to oblique rotators. This point will be discussed in Section 4. In this final section, we also present empirical but useful expressions of the spatial dependence of particle fluxes and $E_\parallel$, together with the relationship between the voltage drop and the current density.

2 PAIR-PRODUCTION CASCADE IN THE OUTER GAP

We first reduce the Poisson equation into a one-dimensional form in Section 2.1. Next, we introduce a model of the power-law background radiation field in Section 2.2. We then present a one-dimensional description of $e^\pm$ and γ-ray distribution functions in Section 2.3, and impose suitable boundary conditions in Section 2.4.

2.1 Reduction of the Poisson equation

As discussed in section 5 of Paper I, transfield structure does not play the primary role in the gap closure problem in the present paper; this contrasts strikingly with CHR, in which the single-signed curvature of field lines results in an exponential growth of particle number densities in the transfield direction of a geometrically thin gap. We therefore consider a one-dimensional gap structure along the field lines for simplicity, neglecting all the transfield dependence of quantities.

Suppose that the magnetic field lines are straight lines parallel to the x-axis (see fig. 1 of Paper I). Here, x is an outwardly increasing coordinate along a magnetic field line. Expanding $\rho_{GJ}(x)$ around the null surface located at the origin, $x = 0$, we can write the Poisson equation in the form

$$-\frac{d^2\Phi}{dx^2} = 4\pi\left[e(N^+ - N^-) - \left(\frac{\partial\rho_{GJ}}{\partial x}\right)_0 x\right], \tag{2}$$

where N_+ and N_- are the spatial number densities of e^+ and e^-, respectively; e refers to the magnitude of the charge on the electron. The subscript 0 indicates that the derivative is evaluated at $x = 0$. (In Section 4, the neglect of transfield derivatives on the left-hand side will be justified in accordance with the small longitudinal gap width.)

As described in Paper I, it is convenient to non-dimensionalize the length-scales by c/ω_p, where the plasma frequency ω_p is defined by

$$\omega_p = \sqrt{\frac{4\pi e^2}{m_e}\frac{\Omega B}{2\pi ce}} = 1.875 \times 10^7 \Omega_2^{1/2} B_5^{1/2} \text{ rad s}^{-1}; \tag{3}$$

the magentic field is evaluated at the null surface such that $B_5 \equiv B/10^5 \text{ G} = 1.76\mu_{30}\Omega_2$, where $\mu_{30} \equiv (\mu/10^{30} \text{ G cm}^3)$ is the dimensionless dipole moment of an aligned rotator. Introducing the dimensionless coordinate variable

$$\xi \equiv \frac{\omega_p}{c}x = 6.25 \times 10^{-4}\Omega_2^{1/2}B_5^{1/2}x, \tag{4}$$

we can simplify the Poisson equation (2) to the form

$$E_\parallel = -\frac{d\varphi}{d\xi} \tag{5}$$

and

$$\frac{dE_\parallel}{d\xi} = n_+(\xi) - n_-(\xi) - A\xi, \tag{6}$$

where the dimensionless electrostatic potential and electric field are defined by

$$\varphi(\xi) \equiv \frac{e\Phi(x)}{m_ec^2}, \tag{7}$$

$$E_\parallel \equiv -\frac{d\varphi}{d\xi} = \frac{e}{m_ec\omega_p}\frac{d\Phi}{dx} \tag{8}$$

$$= 3.12 \times 10^{-5}\left(\frac{d\Phi/dx}{\text{V/m}}\right)\frac{1}{\sqrt{\Omega_2 B_5}}, \tag{9}$$

and the particle densities are normalized in terms of the Goldreich–Julian density,

$$n_\pm(\xi) \equiv \frac{2\pi ce}{\Omega B}N_\pm(x); \tag{10}$$

moreover, A is the dimensionless expansion coefficient of ρ_{GJ} at the null surface and can be estimated as (Paper I)

$$A \equiv \frac{c}{\omega_p}\frac{2\pi c}{\Omega B}\left(\frac{\partial\rho_{GJ}}{\partial x}\right)_0 \approx \frac{c}{\omega_p R_c}$$

$$= 1.1 \times 10^{-5}\Omega_2^{1/2}B_5^{-1/2}\left(\frac{R_c}{0.5r_{LC}}\right)^{-1}. \tag{11}$$

2.2 Background radiation field

Let us briefly describe the background radiation field. We assume that the spectral number density of background radiation per unit energy interval $m_ec^2\epsilon_s \sim m_ec^2(\epsilon_s + d\epsilon_s)$ can be represented by a single power law,

$$\frac{dN_s}{d\epsilon_s} = C(\alpha)\epsilon_s^{-\alpha} \quad (\epsilon_{min} < \epsilon_s < \epsilon_{max}), \tag{12}$$

where $C(\alpha)$ is a decreasing function of α and is defined by

$$C(\alpha) \equiv \frac{2-\alpha}{\epsilon_{max}^{2-\alpha} - \epsilon_{min}^{2-\alpha}}\frac{U_s}{m_ec^2}; \tag{13}$$

ϵ_{max} and ϵ_{min} are the cut-off energy of the spectrum. In what follows, we shall adopt

$$\epsilon_{max} = 10 \text{ keV}/m_ec^2 = 1.95 \times 10^{-2}, \tag{14}$$

$$\epsilon_{min} = 0.1 \text{ eV}/m_ec^2 = 1.95 \times 10^{-5}. \tag{15}$$

Evaluating U_s at the radius $r = 0.67r_{LC}$, which is the intersection of the null surface and the last open field line for an aligned
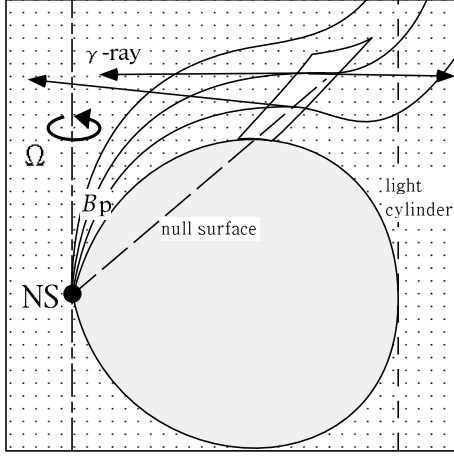
Figure 1. A side view of a hypothetical outer magnetospheric gap which is immersed in a dense soft photon field, which enables γ-ray production via inverse Compton scattering.
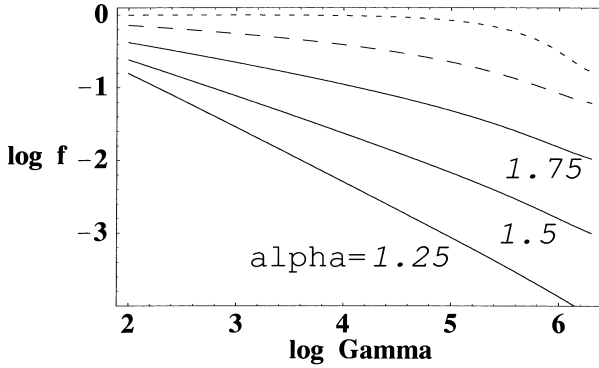

Figure 2. $\log_{10} f(\Gamma)$ versus $\log_{10} \Gamma$. The solid lines represent the cases of $\alpha = 1.25$, 1.5 and 1.75 (from bottom to top), while dashed and dotted lines correspond to $\alpha = 2.0$ and 3.0, respectively.

rotator, we obtain

$$U_s = L_s/[4\pi(0.67 r_{LC})^2 c] = 6.0 \times 10^7 L_{36} \Omega_2^2 \, \text{erg cm}^{-3}, \qquad (16)$$

where $L_{36} \equiv L_s/(10^{36} \, \text{erg s}^{-1})$ is a dimensionless soft photon luminosity. If we adopt $\alpha = 1.5$, for instance, N_s and L_{36} are related by

$$N_s = \frac{1}{\sqrt{\epsilon_{min}\epsilon_{max}}} \frac{U_s}{m_e c^2} = 3.75 \times 10^{17} L_{36} \Omega_2^2 \, \text{cm}^{-3}. \qquad (17)$$

For such a luminous background radiation field, the radiation reaction force resulting from inverse Compton (IC) scattering dominates reaction forces from the curvature radiation and synchrotron radiation (Appendix A).

The IC scattering limits the Lorentz factor of the $e^\pm$ to the value that satisfies

$$e|\text{d}\Phi/\text{d}x| = m_p c \omega_p |E_\parallel| = \sigma_T U_s f(\Gamma, \alpha)\Gamma^2, \qquad (18)$$

where $f(\Gamma,\alpha)$ is the coefficient describing the strength of the Compton drag on a single e^+ or e^-. The coefficient f would be unity if all the soft photons were to be scattered in the Thomson regime. However, it becomes much smaller than unity in practice, especially for large Lorentz factors or for hard spectra of the target

photons (i.e. for small α). We present the derivation of coefficient f in Appendix B, and depict its dependence on Γ and α in Fig. 2. The solid lines, which represent the three cases of $\alpha = 1.25$, 1.5, and 1.75 (from bottom to top), decline with increasing Γ roughly linearly. On the other hand, the dotted line, which represents $f(\Gamma, 3.0)$, stays at ~ 1 for small Γ ($< 10^5$). This is because almost all the photons are scattered in the Thomson regime. We use equations (12), (13) and (16) to calculate the pair-production redistribution function, η_p, in the next subsection.

2.3 Particle and γ-ray Boltzmann equations

The particles in the gap are accelerated by $E_\parallel$ and saturate at the high Lorentz factor computed from equation (18). Therefore, particle velocities are virtually $\pm c$ with vanishing pitch angles (see Appendix A for details). This simplifies the continuity equations of $e^\pm$s significantly. Without loss of any generality, we can assume that the electric field is positive in the gap, in which e^+ (or e^-) move outwards (or inwards). In rectilinear coordinates, their continuity equations then become

$$+c \frac{\text{d}N_+}{\text{d}x} = \int_0^\infty \text{d}\epsilon_\gamma \, \eta_p(\epsilon_\gamma)[G_+(x, \epsilon_\gamma) + G_-(x, \epsilon_\gamma)], \qquad (19)$$

$$-c \frac{\text{d}N_-}{\text{d}x} = \int_0^\infty \text{d}\epsilon_\gamma \eta_p(\epsilon_\gamma)[G_+(x, \epsilon_\gamma) + G_-(x, \epsilon_\gamma)], \qquad (20)$$

where $G_\pm(x,\epsilon_\gamma)$ are the distribution functions of γ-ray photons propagating in the $\pm x$ directions at γ-ray energy $m_e c^2 \epsilon_\gamma$, moreover, η_p is the angle-averaged pair-production redistribution function defined by (Berestetskii, Lifshitz & Pitaevskii 1989)

$$\eta_p(\epsilon_\gamma) \equiv \frac{c\sigma_T}{2} \int_{-1}^1 \text{d}\mu \int_{2/(1-\mu)\epsilon_\gamma}^{\epsilon_{max}} \text{d}\epsilon_s \frac{\text{d}N_s}{\text{d}\epsilon_s} \frac{1}{\lambda_p(v)}, \qquad (21)$$

$$\frac{1}{\lambda_p(v)} \equiv \frac{3}{16}(1 - v^2)\left[(3 - v^4)\ln\frac{1+v}{1-v} - 2v(2 - v^2)\right], \qquad (22)$$

$$v(\epsilon_\gamma, \epsilon_s, \mu) \equiv \sqrt{1 - \frac{2}{1-\mu}\frac{1}{\epsilon_\gamma\epsilon_s}}, \qquad (23)$$

where μ is the cosine of the colliding angle of the soft and the hard photons.

Let us introduce a discrete form of γ-ray densities with a system of grids β_i in ϵ_γ space such that

$$g_\pm^i(\xi) \equiv \frac{2\pi ce}{\Omega B} \int_{\beta_{i-1}}^{\beta_i} \text{d}\epsilon_\gamma G_\pm(x, \epsilon_\gamma). \qquad (24)$$

We are concerned here only with γ-ray photons that can materialize as pairs. Therefore, we set $\beta_0 = 1/\epsilon_{max}$, which corresponds to the lowest γ-ray energy, $h\nu = \beta_0 m_e c^2 = 26.2 \, \text{MeV}$. To cover a wide range of γ-ray energies, we divide the γ-ray spectra into 12 energy bins, that is $\beta_1 = 3.0/\epsilon_{max}$, $\beta_2 = 1.0 \times 10^1/\epsilon_{max}$, $\beta_3 = 3.0 \times 10^1/\epsilon_{max}$, $\beta_4 = 1.0 \times 10^2/\epsilon_{max}$, $\beta_5 = 3.0 \times 10^2/\epsilon_{max}$, $\beta_6 = 1.0 \times 10^3/\epsilon_{max}$, $\beta_7 = 3.0 \times 10^3/\epsilon_{max}$, $\beta_8 = 1.0 \times 10^4/\epsilon_{max}$, $\beta_9 = 3.0 \times 10^4/\epsilon_{max}$, $\beta_{10} = 1.0 \times 10^5/\epsilon_{max}$, $\beta_{11} = 3.0 \times 10^5/\epsilon_{max}$, $\beta_{12} = 1.0 \times 10^6/\epsilon_{max}$. As will be shown in Section 3.2, most of the γ-ray photons have energies less than $h\nu = \beta_{10} m_e c^2 = 2.62 \, \text{TeV}$.

We can rewrite equations (19) and (20) in the dimensionless

forms

$$\frac{dn_+}{d\xi} = +\sum_{i=1}^{14} \eta_p^i [g_+^i(\xi) + g_-^i(\xi)], \tag{25}$$

$$\frac{dn_-}{d\xi} = -\sum_{i=1}^{14} \eta_p^i [g_+^i(\xi) + g_-^i(\xi)], \tag{26}$$

where η_p^i are evaluated at the central energy in each bin and are defined as

$$\eta_p^i \equiv \frac{1}{\omega_p} \eta_p \left(\frac{\beta_{i-1} + \beta_i}{2} \right); \tag{27}$$

$n_\pm(\xi) \equiv (2\pi c e / \Omega B) N_\pm(x)$ is normalized with the same factor as $g_\pm^i(\xi)$.

A combination of equations (25) and (26) yields the current conservation law,

$$j_0 \equiv n_+(\xi) + n_-(\xi). \tag{28}$$

When $j_0 = 1.0$, the current density equals the Goldreich–Julian current density, $\Omega B/(2\pi)$.

Let us next discuss the Boltzmann equations that the γ-ray distribution functions obey. In accordance with the one-dimensional approximation, we can write the γ-ray Boltzmann equations in form

$$\pm c \frac{\partial}{\partial x} G_\pm(x, \epsilon_\gamma) = -\eta_p G_\pm(x, \epsilon_\gamma) + \eta_{IC} N_\pm(x), \tag{29}$$

where $\eta_{IC}(\epsilon_\gamma, \Gamma)$ is the Compton redistribution function, defined by (see equation B1 and the explanation below)

$$\eta_{IC} \equiv c \int_{\epsilon_{min}}^{\epsilon_{max}} d\epsilon_s \frac{dN_s}{d\epsilon_s} \sigma_c(\epsilon_s \Gamma) \delta[\epsilon_\gamma - \min(\Gamma^2 \epsilon_s, \Gamma)]; \tag{30}$$

$$\sigma_c(z) \equiv \frac{3}{4}\sigma_T \left\{ \frac{1+z}{z^3} \left[\frac{2z(1+z)}{1+2z} - \ln(1+2z) \right] \right.$$
$$\left. + \frac{\ln(1+2z)}{2z} - \frac{1+3z}{(1+2z)^2} \right\}. \tag{31}$$

Integrating equation (29) in the energy intervals $[m_e c^2 \beta_{i-1}, m_e c^2 \beta_i]$, we obtain

$$\pm \frac{d}{d\xi} g_\pm^i(\xi) = -\eta_p^i g_\pm^i(\xi) + \eta_{IC}^i n_\pm(\xi), \tag{32}$$

where $i = 1, 2, \ldots, m$ and

$$\eta_{IC}^i \equiv \frac{1}{\omega_p} \int_{\beta_{i-1}}^{\beta_i} d\epsilon_\gamma \eta_{IC}(\epsilon_\gamma, \Gamma) \tag{33}$$

denotes the number of γ-ray photons scattered by a single e^+ or e^- in the normalization length-scale c/ω_p between dimensionless energy intervals β_{i-1} and β_i.

2.4 Boundary conditions

To solve the differential equations (5), (6), (25), (26) and (32), we must impose boundary conditions.

Let us first consider the conditions at the *inner* (starward) boundary $\xi = \xi_1$. In the same manner as we considered the electrostatics in Paper I, we impose

$$E_\parallel(\xi_1) = 0 \tag{34}$$

and

$$\varphi(\xi_1) = 0. \tag{35}$$

We further hypothesize that neither γ-ray photons nor particles enter from the outside of the gap, that is

$$g_+^i(\xi_1) = 0 \quad (i = 1, 2, \ldots, m), \tag{36}$$

and

$$n_+(\xi_1) = 0, \tag{37}$$

which yields, with the help of the charge conservation law (28),

$$n_-(\xi_1) = j_0. \tag{38}$$

We next consider the conditions at the *outer* boundary ($\xi = \xi_2$), which is defined so that $E_\parallel$ vanishes again:

$$E_\parallel(\xi_2) = 0. \tag{39}$$

In the same manner, at $\xi = \xi_1$, we impose both

$$g_-^i(\xi_2) = 0 \quad (i = 1, 2, \ldots, m) \tag{40}$$

and

$$n_-(\xi_2) = 0. \tag{41}$$

To sum up, we have $2m + 6$ boundary conditions in total (34)–(41) for $2m + 4$ differential equations; thus two extra boundary conditions must be compensated for by making the positions of the boundaries, $\xi = \xi_1$ and ξ_2, free.

It follows from the basic equations (5), (6), (25), (26) and (32) that the gap structure is described by the following four parameters:

$$j_0 \equiv n_+ + n_-, \tag{42}$$

$$\eta_{IC}^i, \eta_p^i \propto L_{36} \Omega_2^{3/2} B_5^{-1/2}, \tag{43}$$

$$\frac{R_c}{c/\omega_p} \propto \frac{R_c}{r_{LC}} \sqrt{\frac{B}{\Omega}} \tag{44}$$

and

$$\alpha. \tag{45}$$

The reader may notice here that equation (18) gives $|E_\parallel| \propto L_{36} \Omega_2^{3/2} B_5^{-1/2} f(\Gamma, \alpha) \Gamma^2$, which implies that Γ is related to $E_\parallel$ through the second parameter alone. Moreover, even though γ-ray photons are produced via IC scatterings, the curvature radius appears through the expansion coefficient A in equation (11).

3 STRUCTURE OF THE OUTER GAP

In Sections 3.1 and 3.2, we investigate how the solutions depend on the dimensionless current density, j_0. We then describe the dependence on the pair-production mean free path, $\propto 1/L_{36}$, in Section 3.3 and that on the photon index, α, in Section 3.4.

3.1 Longitudinal electric field

To aid in grasping the basic features, we first show some examples of the solutions of $E_\parallel(\xi)$ for several values of the 'first' parameter j_0 (see equation 42). In Fig. 3, the dotted, dashed and solid lines correspond to $j_0 = 0.04588$, 0.02 and 0.01, respectively. Other parameters are fixed at $\Omega_2 = 1.0$, $\mu_{30} = 1.0$, $L_{36} = 3.0$ and $\alpha = 1.5$.

For very small j_0, the charge density ($n_+ - n_-$ term) in equation (6) does not contribute. As a result, equation (6) gives
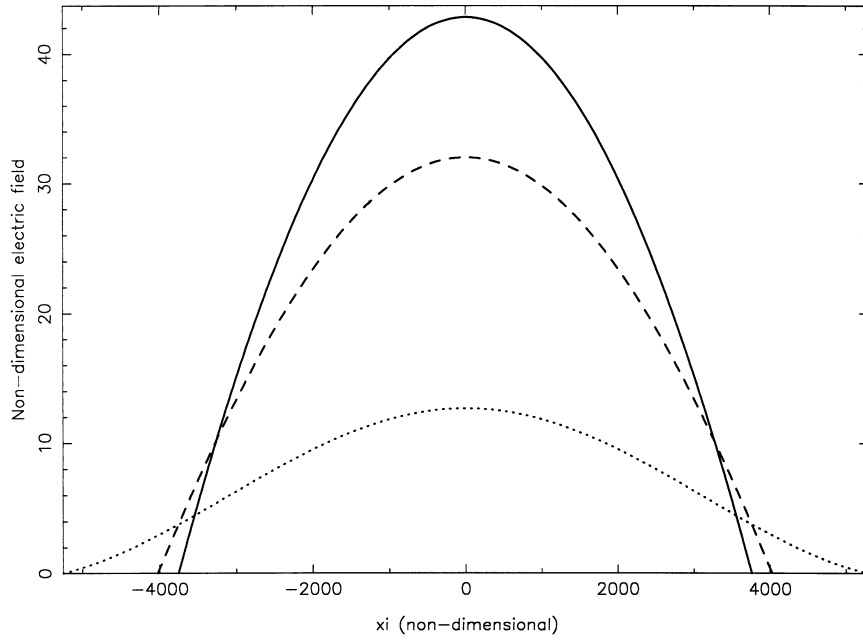
Figure 3. Examples of longitudinal electric field $E_\parallel(x)$. The dotted, solid and dashed lines represent the solutions corresponding to $j_0 = 0.0433, 0.02$ and 0.01 respectively. Other parameters are fixed at $\Omega_2 = 1.0$, $\mu_{30} = 1.0$ and $L_{36} = 3.0$ throughout the gap. $x = 1.2 \times 10^3 \xi$ cm.

approximately a quadratic solution, $E_\parallel(\xi) = E_\parallel(0) - (A/2)\xi^2$, which is represented by the solid line in Fig. 3.

However, as j_0 increases, $E_\parallel(\xi)$ deviates from the quadratic form to have a 'brim' at the boundaries. Finally, at a certain value $j_0 = j_{cr}$, the derivative of $E_\parallel$ vanishes at the boundaries. In the case of $\Omega_2 = 1.0$, $\mu_{30} = 1.0$, $L_{36} = 3.0$, j_{cr} equals 0.0433, for which the solution is represented by the dotted line in Fig. 3. Above the critical current density, j_{cr}, there are no solutions satisfying the $2m + 6$ boundary conditions presented in Section 2.5 (see fig. 2 of Hirotani & Okamoto 1998).

It will also be useful to describe the Lorentz factor $\Gamma(\xi)$. The results are presented in Fig. 4; the parameters are the same as we have chosen in Fig. 3. It is plain from this figure that the Lorentz factor does not exceed 10^6; therefore, the assumption that the γ-ray photons are primarily produced via inverse Compton scatterings is self-consistently satisfied (see equation A4 and the discussion below).

3.2 Particle and γ-ray fluxes

Let us devote a little more space to examining $n_\pm(\xi)$ and $g_\pm(\xi)$. First, examples of n_+ (thick curves) and n_- (thin curves) are drawn in Fig. 5. Parameters are chosen to be the same as in Fig. 3. We can easily see that particles distribute symmetrically with respect to $\xi = 0$ in the sense that $n_+(\xi) = n_-(-\xi)$. This is because the small gap width ($H \ll r_{LC}$) prevents the appearance of two-dimensional effects (or transfield structure) in the Poisson equation (see the explanation in Section 4.1 of Paper I).

Secondly, examples of $\log_{10} g_+$ and $\log_{10} g_-$ are shown in Fig. 6. The thick curves denote the fluxes of g_+, while the thin curves denote those of g_-. The γ-ray distribution is also symmetric with respect to $\xi = 0$. The solid lines correspond to the lowest energy bin, $1/\epsilon_{max} < \epsilon_\gamma < 10^2/\epsilon_{max}$, while the dashed and dash–dotted lines correspond to $10^2/\epsilon_{max} < \epsilon_\gamma < 10^3/\epsilon_{max}$, $10^3/\epsilon_{max} < \epsilon_\gamma < 10^4/\epsilon_{max} = 5.11 \times 10^5$, respectively. Above the energy

$5.11 \times 10^5 m_e c^2$, no γ-ray photons are produced, because all the $e^\pm$ have energies less than this value, as indicated by the Lorentz factors in Fig. 4. Current density is fixed at $j_0 = 0.01$. We can also see from Fig. 6 that each e^+/e^- produces $N_\gamma \equiv g_+/n_+ \sim 6$ γ-ray photons via IC scattering.

3.3 Dependence on the soft photon luminosity

In this subsection, we are concerned with the dependence of the solutions on the second parameter, η^i_{IC}, $\eta^i_p \propto L_s$. In Fig. 7 we present the solutions of $E_\parallel(\xi)$. The dashed, solid and dotted lines correspond to $L_{36} = 10.0, 3.0$ and 1.0, respectively. Other parameters are fixed at $\alpha = 1.5$, $j_0 = 0.01$, $\Omega_2 = 1.0$, $\mu_{30} = 1.0$.

It is plain from Fig. 7 that the longitudinal electric field increases with decreasing soft photon luminosity, L_s. This result is deeply associated with the fact that $H (\equiv \xi_2 - \xi_1)$ is a decreasing function of L_s, because the quadratic solution $E_\parallel(\xi) = E_\parallel(0) - (A/2)\xi^2$ gives $E_\parallel(0) = AH^2/8$.

The results of H versus j_0 and L_{36} are summarized in Fig. 8. The dashed, solid and dotted lines correspond to the cases of $L_{36} = 10.0, 3.0$ and 1.0, respectively. Other parameters are fixed at $\alpha = 1.5$, $\Omega_2 = 1.0$ and $\mu_{30} = 1.0$. This figure shows that H increases with decreasing luminosity. Compared with Paper I, in which γ-ray photons are produced via curvature radiation, the dependence of H on L_s, and hence $E_\parallel$ on L_s, is very strong. This is because the soft photon luminosity affects pair production alone if γ-rays are produced via curvature process but it affects both pair and γ-ray production if they are produced via IC scattering.

The condition that the gap width should be much greater than the IC mean free path is self-consistently satisfied for all of the three cases. (If it were to break down, synchrotron radiation could become important.) For example, gap width becomes $\sim 0.035 r_{LC}$ for $L_{36} = 10.0$, while $\lambda_{IC} \sim 0.001 r_{LC}$.

Integrating $E_\parallel$ along the field line from $\xi = \xi_1$ to ξ_2, we can calculate the voltage drop, V_{drop}, in the accelerator. The results are
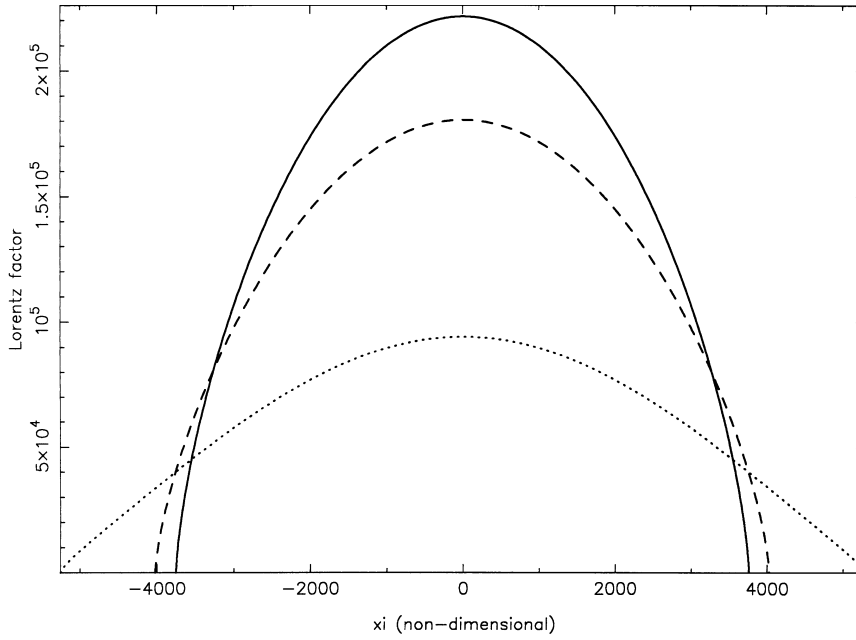
Figure 4. Examples of the Lorentz factor $\Gamma(\xi)$. The solid, dashed and dotted lines correspond to the same parameters chosen in Fig. 3. $x = 1.2 \times 10^3 \xi$ cm.
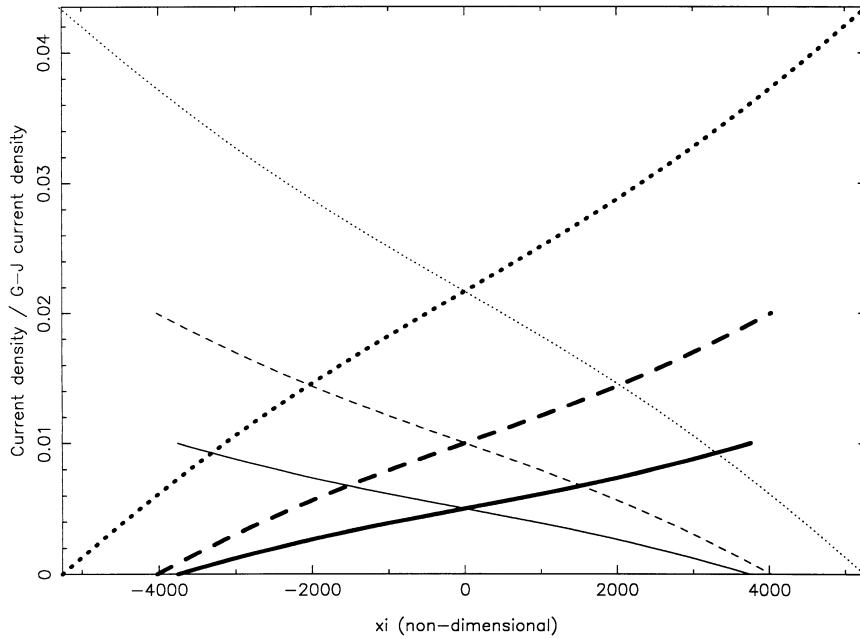

Figure 5. Examples of $n_+(\xi)$ (thick curves) and $n_-(\xi)$ (thin curves). The solid, dashed and dotted lines correspond to the same parameters chosen in Fig. 3. $x = 1.2 \times 10^3 \xi$ cm.

summarized in Fig. 9. The solid line describes $V_{\mathrm{gap}}(j_0)$ for $L_{36} = 3.0$, while the dashed and dotted lines are for $L_{36} = 10.0$ and 1.0, respectively. Other parameters are fixed at $\alpha = 1.5$, $\Omega_2 = 1.0$ and $\mu_{30} = 1.0$.

This figure indicates that the voltage drop in the gap increases with decreasing L_{36}. This conclusion is qualitatively consistent with the results obtained in Paper I. However, in the current paper the luminous X-ray field, which reduces the pair-production mean free path and hence the gap width, leads to a small voltage drop in the gap, compared with Paper I.

3.4 Dependence on the photon index

Let us finally investigate the relationship between the voltage drop and the photon index, α. We summarize the result in Fig. 10. The solid line corresponds to $V_{\mathrm{gap}}(j_0)$ for $\alpha = 1.5$, while the dashed line is for $\alpha = 1.625$. Other parameters are fixed at $\Omega_2 = 1.0$, $L_{36} = 3.0$ and $\mu_{30} = 1.0$.

It is plain that V_{drop} decreases with increasing α when L_s is fixed. This is because the gap width, which essentially describes the voltage drop, decreases with increasing number density of
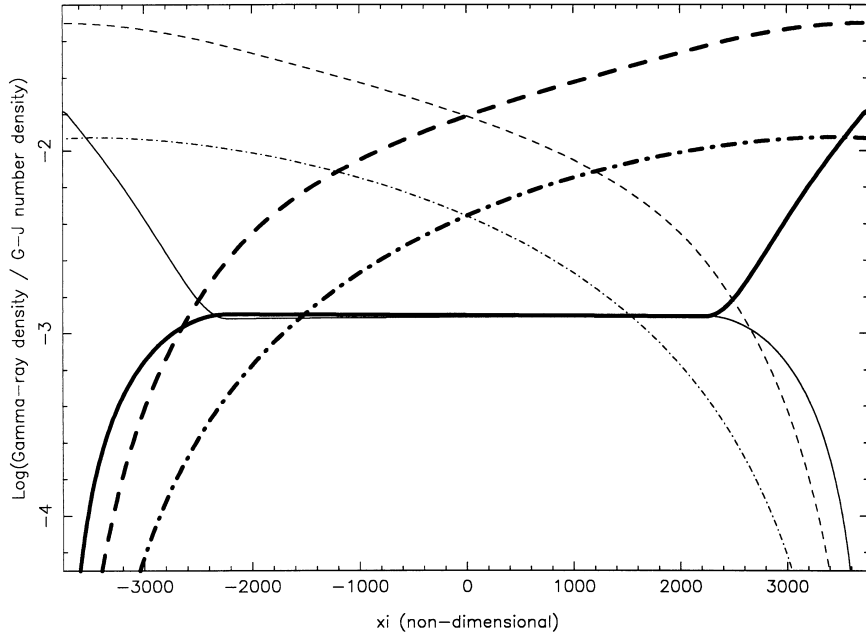
Figure 6. Examples of $\log_{10} g_+(\xi)$ (thick curves) and $\log_{10} g_-(\xi)$ (thin curves). The solid lines correspond to the lowest energy bin, while the dashed, dash–dotted and dotted lines correspond to higher energy bins (see text for details). $x = 1.2 \times 10^3 \xi$ cm.
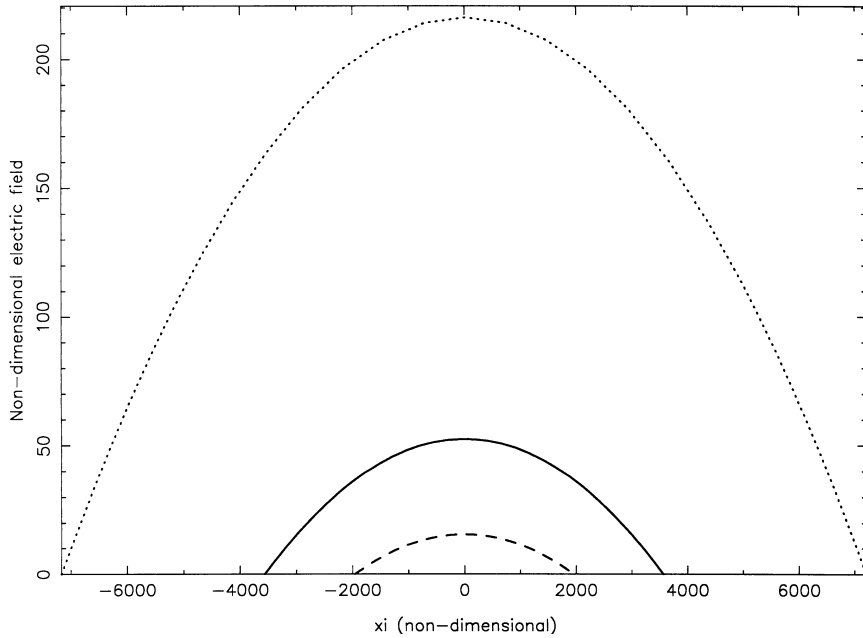

Figure 7. Longitudinal electric field $E_\parallel(x)$ in the case when $j_0 = 0.01$, $\Omega_2 = 1.0$ and $\mu_{30} = 1.0$. The dashed, solid and dotted lines represent the solutions corresponding to $L_{36} = 10.0$, 3.0 and 1.0, respectively. $x = 1.2 \times 10^3 \xi$ cm.

target photons, or equivalently with decreasing mean free path for pair production.

4 DISCUSSION

In summary, we have developed a one-dimensional model for an outer gap accelerator immersed in a luminous radiation field in which $e^\pm$s lose their perpendicular momentum soon after their birth owing to inverse Compton (IC) scattering. As a result, synchrotron radiation is not important in γ-ray production. The terminal Lorentz factor becomes $(\sim 1\text{–}3) \times 10^5$, for which IC scattering dominates curvature radiation in γ-ray production. A e^+ or e^- produces typically 10 γ-ray photons that can materialize as pairs. The pair-production mean free path, and hence gap width, increases with decreasing background radiation field. What is most important is that the voltage drop, V_{gap}, is only 0.01 per cent of the available electromotive force produced on the spinning
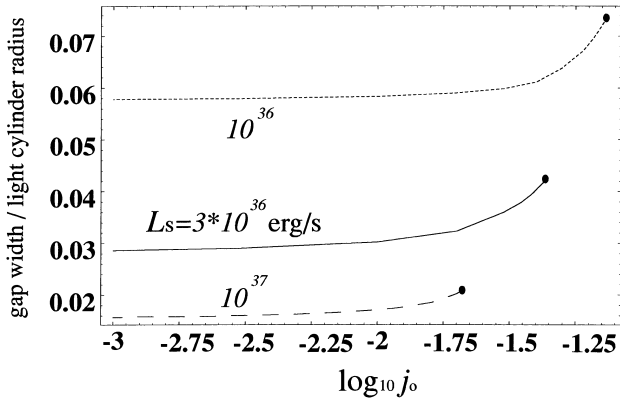
Figure 8. Gap width $(c/\omega_p)H/r_{LC}$ versus $\log_{10} j_0$. The solid line describes the gap width for $L_{36} = 3.0$, while the dashed and dotted lines are for $L_{36} = 10.0$ and 1.0, respectively. The filled circles indicate the points where j_0 coincides with j_{cr}, above which no solutions exist.
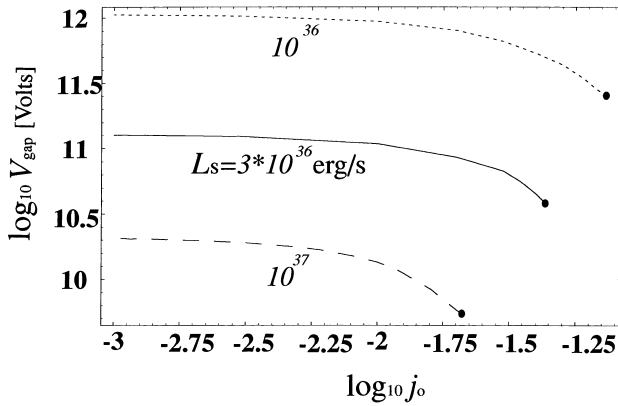

Figure 9. $\log_{10} V_{gap}[V]$ versus $\log_{10} j_0$. The solid line describes $V_{gap}(j_0)$ for $L_{36} = 3.0$, while the dashed and dotted lines are for $L_{36} = 10.0$ and 1.0, respectively. The filled circles indicates the points where j_0 coincides with j_{cr}, above which no solutions exist.
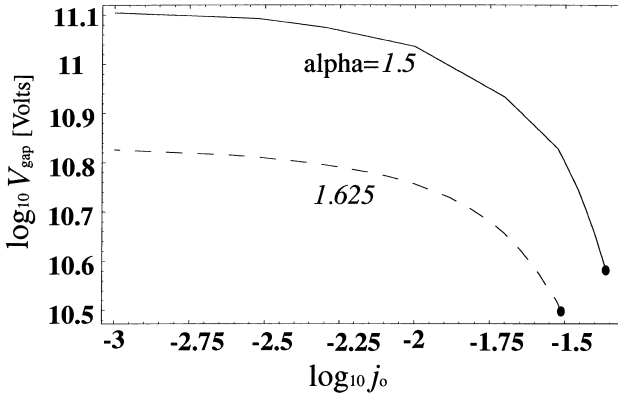

Figure 10. $\log_{10} V_{gap}[V]$ versus $\log_{10} j_0$. The solid line describes $V_{gap}(j_0)$ for $\alpha = 1.5$, while the dashed line is for $\alpha = 1.625$. The filled circles indicate the points where j_0 coincides with j_{cr}, above which no solutions exist.

neutron star surface ($\sim 10^{16}$ V) even for the low-luminosity case of $L_s = 10^{36}$ erg s^{-1}. The voltage drop decreases with increasing L_s.

Even though we have assumed an axial symmetry, the discussion and results are not tied to the case of an aligned rotator. This is because the gap structure is described by the local

soft photon field, current density and local magnetic field, which appears through the expansion coefficient of ρ_{GJ}, A, in equation (11). As the dense soft photon field is assumed to be isotropic, collision angles and hence pair-production rate are independent of the inclination between the rotational and magnetic axes. As a result, the inclination affects the system through A alone, which is well approximated by $A \approx c/(\omega_p R_c)$ (equation 11) for a moderate inclination. On these grounds, the essential properties demonstrated in this paper are not tied to the aligned case.

We discuss the validity of the neglect of transfield dependence in the Poisson equation. In CHR's model, a very small transfield thickness was hypothesized to avoid γ-ray penetration into the gap. However, in the present model, the transfield thickness can be reasonably large ($> 0.1 r_{LC}$, say), because the gap is maintained when it is irradiated by γ-ray photons. Therefore, the smallness of the longitudinal width, as indicated by Fig. 8, justifies the neglect of transfield derivatives in the Poisson equation.

Let us next discuss the approximate expressions for $n_\pm(\xi)$, $E_\parallel(\xi)$ and $V_{gap}(j_0)$. First, if we were to redraw Fig. 3 by renormalizing the abscissa by $b(j_0) \equiv H(j_0)/2$ and the ordinate by j_0, we would find that the distributions of $n_+(\xi/b)/j_0$ and $n_-(\xi/b)/j_0$ for the three cases almost coincide. As an approximate but general expression, we find

$$n_+ \approx \frac{j_0}{2}\left\{\frac{\xi}{b(j_0)} + 1 - \epsilon \sin\left[\pi \frac{\xi}{b(j_0)}\right]\right\}, \tag{46}$$

$$n_- \approx \frac{j_0}{2}\left\{-\frac{\xi}{b(j_0)} + 1 + \epsilon \sin\left[\pi \frac{\xi}{b(j_0)}\right]\right\}, \tag{47}$$

where the small coefficient $\epsilon \approx 0.09$ has little dependence on j_0, Ω_2, B_5 or L_{36}. Amazingly, these approximate expressions are valid not only when IC scattering dominates but also when curvature radiation does. In other words, if we redrew Fig. 3 in Paper I on a linear scale, we would find that expressions (46) and (47) are also applicable.

Secondly, substituting expressions (46) and (47) into Poisson equation (6), we obtain

$$E_\parallel = \frac{j_0 - bA}{2b(j_0)}(\xi^2 - b^2) + \frac{\epsilon b(j_0) j_0}{\pi}\left\{1 + \cos\left[\pi \frac{\xi}{b(j_0)}\right]\right\}. \tag{48}$$

For $j_0 = j_{cr} = b(j_{cr})A$, $E_\parallel$ varies sinusoidally with ξ as

$$E_\parallel = \frac{\epsilon b(j_{cr}) j_{cr}}{\pi}\left\{1 + \cos\left[\pi \frac{\xi}{b(j_{cr})}\right]\right\}. \tag{49}$$

Examples are presented by the dotted line in Fig. 3 of this paper and in fig. 3 of Paper I. A slight deviation of the dotted lines from the sinusoidal form represents the difference of the approximated expressions (46) and (47) from the true profile.

Thirdly, integrating (48) over ξ from $-b$ to b, we obtain the voltage drop in the gap. The result is

$$V_{gap}(j_0) = -\frac{2}{3}b^2(j_0)\left(j_{cr} - j_0 + \frac{3\epsilon}{\pi}j_0\right). \tag{50}$$

The gap width, $2b(j_0)$, is presented in Fig. 9. Substituting typical values of $b(j_0)$ and $\epsilon \approx 0.09$ into equation (50), we can approximately compute the voltage drop, V_{gap}. For very small current densities $j_0 \ll j_{cr}$, V_{gap} is kept constant at a value

$$|V_{gap}| = V_{max} = \frac{2}{3}b^3(j_0)A. \tag{51}$$

We point out here that the gap width $2b(j_0)$ is kept constant for

small j_0, as Fig. 8 indicates. On the other hand, at $j_0 = j_{cr}$, $|V_{gap}|$ becomes minimum at the value

$$|V_{gap}| = V_{min} = \frac{3\epsilon}{\pi} \cdot \frac{2}{3} b^3(j_{cr}) A. \tag{52}$$

It follows that the ratio becomes

$$\frac{V_{min}}{V_{max}} = \frac{3\epsilon}{\pi} \times \left[\frac{b(j_{cr})}{b(j_0)} \right]^3. \tag{53}$$

Equations (46)–(53) hold not only when the IC scattering dominates but also when the curvature radiation dominates.

Let us finally check the validity of equation (53). As an example, we consider the case of $L_{36} = 3.0$ and $\alpha = 1.5$. In this case, the numerical values of the gap width become

$$2b(j_0) = 7.12 \times 10^3, \quad 2b(j_{cr}) = 1.06 \times 10^4 \tag{54}$$

in dimensionless units. Substituting these values into (53), we obtain

$$\frac{V_{min}}{V_{max}} \approx 0.28, \tag{55}$$

where $\epsilon \approx 0.09$ is substituted. This value is roughly consistent with the numerical value

$$\frac{V_{min}}{V_{max}} = \frac{3.82 \times 10^{10}\,\mathrm{V}}{1.30 \times 10^{11}\,\mathrm{V}} = 0.293, \tag{56}$$

which reinforces the validity of equations (46)–(48) and (50).

ACKNOWLEDGMENTS

REFERENCES

Berestetskii V. B., Lifshitz E. M., Pitaevskii L. P., 1989, Quantum Electrodynamics. Nauka, Moscow
Beskin V. S., Istomin Ya N., Par'ev V. I., 1992, Sva, 36, 642
Chen K. S., Ho C., Ruderman M., 1986a, ApJ, 300, 500
Chen K. S., Ho C., Ruderman M., 1986b, ApJ, 300, 522
Goldreich P., Julian W. H., 1969, ApJ, 157, 869
Hirotani K., Okamoto I., 1998, ApJ, 497, 563
Hirotani K., Shibata S., 1999, MNRAS, (Paper I, this issue) 308, 54
Holloway N. J., 1973, Nat, 246, 6
Michel C. F., 1998, in Shibazaki N., Kawai N., Shibata S., Kifune T., eds, Neutron Stars and Pulsars. Universal Academy Press, Tokyo, p. 263
Romani R. W., 1996, ApJ, 470, 469

APPENDIX A: RADIATION REACTION FORCES

In this appendix, we show that IC scattering is the dominant process in γ-ray production. In the present paper, we consider a luminous soft photon field such that $U_s > 10^7\,\mathrm{erg\,cm^{-3}}$, which is applicable for gamma-ray pulsars such as the Crab. For such a luminous X-ray radiation field, the radiation reaction force resulting from curvature radiation is negligibly small compared with that resulting from inverse Compton (IC) scattering. To see this, let us take the ratio of P_{curv}/P_{IC}, where P_{curv}/c and P_{IC}/c

denote the radiation reaction forces resulting from curvature radiation and IC scattering, respectively. By estimating the typical curvature radius of the magnetic field lines to be $0.5r_{LC}$, we obtain

$$\frac{P_{curv}}{c} = \frac{8e^2\Gamma^4}{3r_{LC}^2}. \tag{A1}$$

The radiation reaction force resulting from IC scattering is given by

$$\frac{P_{IC}}{c} \approx cN_s\sigma_{KN}\frac{\Gamma m_e c^2}{c} > 50 m_e c^2 N_s \sigma_T, \tag{A2}$$

where σ_{KN} and σ_T are the Klein–Nishina and Thomson cross-sections, respectively. The inequality comes from the fact that

$$\sigma_{KN} \approx \frac{3}{8}\frac{\sigma_T}{\Gamma\epsilon_s}(\ln 2\Gamma\epsilon_s + 0.5) \approx \frac{\sigma_T}{\Gamma\epsilon_s} \tag{A3}$$

when $\Gamma\epsilon_s \gg 1$. Combining the foregoing equations, we have

$$\frac{P_{curv}}{P_{IC}} < 0.67 \left(\frac{\Gamma}{10^6} \right)^4 L_{36}^{-1}. \tag{A4}$$

Remembering that equation (A2) is the severest estimate for the lower limit of P_{IC}/c, we can see from equation (A4) that curvature radiation processes are negligible compared with IC processes unless Γ greatly exceeds 10^6.

Let us next show that synchrotron radiation is negligible in a luminous soft photon field such as $U_s > 10^7\,\mathrm{erg\,cm^{-3}}$. The IC mean free path can be estimated as

$$\frac{\lambda_{IC}}{r_{LC}} = 1.33 \times 10^{-2} L_{36}^{-1} \Omega_2^{-1}. \tag{A5}$$

It follows that $e^\pm$ lose their perpendicular momenta by IC scattering before migrating a few per cent of r_{LC}. However, their longitudinal momenta will soon recover, owing to $E_\parallel$ acceleration, with acceleration length

$$\frac{\lambda_{acc}}{r_{LC}} = \frac{\Gamma m_e c^2}{e|d\Phi/dx|}\frac{1}{r_{LC}} = 1.70 \times 10^{-3} \left(\frac{\Gamma}{10^6} \right) \left(\frac{|d\Phi/dx|}{10^8\,\mathrm{V/m}} \right)^{-1} \Omega_2^{-1}. \tag{A6}$$

As a result, after many scatterings, their pitch angles evolve to such small values that synchrotron radiation is negligible.

It may worth noting that the acceleration length, λ_{acc}, which is defined by equation (A6), is comparable with the gap width, $(c/\omega_p)H$, for $L_{36} = 10.0$ (Fig. 8). Therefore, the assumption of mono-energetic distribution of particle energy is marginally satisfied for $L_{36} = 10.0$. For less luminous cases ($L_{36} < 10.0$), their larger gap width, which leads to larger $E_\parallel$ and hence smaller λ_{acc}, ensures the validity of the mono-energetic approximation, because $\lambda_{acc} \ll (c/\omega_p)H$ holds.

On these gounds, in the first-order approximation, we may regard all the $e^\pm$ as migrating with the same terminal Lorentz factor calculated from equation (18).

APPENDIX B: EQUILIBRIUM LORENTZ FACTOR

We demonstrate the method of deriving the function $f(\Gamma, \alpha)$, which appears in equation (18) and is depicted in Fig. 2. The momentum transfer from a single e^+/e^- to a single photon in a scattering can be approximated by

$$\Delta P \approx \frac{1}{c}\min(\Gamma^2 m_e c^2 \epsilon_s, \Gamma m_e c^2). \tag{B1}$$

For small Γ, the energy transfer will be proportional to Γ^2 on average, while for large Γ it saturates at the kinetic energy of the

particle. Multiplying the collisional frequency in (B1), we can evaluate the drag force resulting from IC scattering as

$$\frac{1}{c}P_{\mathrm{IC}} = \int_{\epsilon_{\mathrm{min}}}^{1/\Gamma} d\epsilon_{\mathrm{s}}\, \frac{dN_{\mathrm{s}}}{d\epsilon_{\mathrm{s}}}\, \sigma_{\mathrm{KN}}\Gamma^2 m_{\mathrm{e}}c^2\epsilon_{\mathrm{s}} + \int_{1/\Gamma}^{\epsilon_{\mathrm{max}}} d\epsilon_{\mathrm{s}}\, \frac{dN_{\mathrm{s}}}{d\epsilon_{\mathrm{s}}}\, \sigma_{\mathrm{KN}}\Gamma m_{\mathrm{e}}c^2.$$

(B2)

We implicitly assumed here that Γ is not too large to satisfy $\Gamma^2\epsilon_{\mathrm{min}} > \Gamma$. In other words, equation (B2) is valid for $\Gamma < \epsilon_{\mathrm{min}}^{-1} = 5.11 \times 10^6$. Substituting the expression for the Klein–Nishina cross-section (equation 31), and equating P_{IC}/c with $e|\mathrm{d}\Phi/\mathrm{d}x|$, we obtain the numerical results presented in Fig. 2.

This paper has been typeset from a TEX/LATEX file prepared by the author.